X-ray luminescence imaging for small animals

Michael C Lun[1], **Wenxiang Cong**[2], **Md. Arifuzzaman**[3], **Meenakshi Ranasinghe**[3], **Sriparna Bhattacharya**[4], **Jeffery Anker**[3,5], **Ge Wang**[2], **Changqing Li**[1,*]

[1]Department of Bioengineering, University of California, Merced, Merced, CA 95343, USA

[2]Department of Biomedical Engineering, Biomedical Imaging Center, Center for Biotechnology and Interdisciplinary Studies, Rensselaer Polytechnic Institute, Troy, NY 12180, USA

[3]Department of Chemistry, Clemson University, Clemson, SC 29634, USA

[4]Clemson Nanomaterials Institute, Department of Physics & Astronomy, Clemson University, Clemson, SC 29634, USA

[5]Department of Bioengineering, Center for Optical Materials Science and Engineering Technology (COMSET), and Institute of Environment Toxicology (CU-ENTOX), Clemson University, Clemson, SC 29634, USA

Abstract

X-ray luminescence imaging emerged for about a decade and combines both the high spatial resolution of x-ray imaging with the high measurement sensitivity of optical imaging, which could result in a great molecular imaging tool for small animals. So far, there are two types of x-ray luminescence computed tomography (XLCT) imaging. One uses a pencil beam x-ray for high spatial resolution at a cost of longer measurement time. The other uses cone beam x-ray to cover the whole mouse to obtain XLCT images at a very short time but with a compromised spatial resolution. Here we review these two methods in this paper and highlight the synthesized nanophosphors by different research groups.

We are building a focused x-ray luminescence tomography (FXLT) imaging system, developing a machine-learning based FXLT reconstruction algorithm, and synthesizing nanophosphors with different emission wavelengths. In this paper, we will report our current progress from these three aspects. Briefly, we mount all main components, including the focused x-ray tube, the fiber detector, and the x-ray tube and x-ray detector for a microCT system, on a rotary which is a heavy-duty ring track. A microCT scan will be performed before FXLT scan. For a FXLT scan, we will have four PMTs to measure four fiber detectors at two different wavelengths simultaneously for each linear scan position. We expect the spatial resolution of the FXLT imaging will be around 100 micrometers and a limit of detection of approximately 2 μg/mL (for $Gd_2O_2S:Eu$).

Keywords

---

*Corresponding Author: Changqing Li, Tel.: (209) 228-4777; cli32@ucmerced.edu.

1. Introduction

Within the last decade, the concept of x-ray-induced luminescence imaging (XLI) has emerged and demonstrated great potential for the molecular imaging in small-animals by combining the high-spatial resolution of traditional x-ray imaging and the superb measurement sensitivity of optical imaging. Specifically, x-ray luminescence computed tomography (XLCT) imaging is a powerful imaging modality capable of high-resolution imaging of deeply embedded x-ray excitable contrast agents in three-dimensions (3D). In principle, x-ray photons are used to penetrate samples deeply, with negligible scatter, and x-ray excitable contrast agents within the path of the excitation beam will absorb the x-ray energy, causing a cascade of events, eventually leading to the emission of many optical photons which pass through the tissue and escape from the skin. Highly sensitive photodetectors, such as an electron multiplying charge-coupled device (EMCCD) camera, can then detect the optical photons for image reconstruction. Pratx *et al.* first reported a selective-excitation based XLCT imaging [1–2] and demonstrated that the distribution of deeply embedded contrast agents could be recovered with high-resolution and sensitivity with this method. Soon following, several research groups, including our own efforts, have pursued and made much progress towards improving XLCT imaging from several aspects through the development and improvement of XLCT imaging systems [3–13], robust reconstruction algorithms [4, 15], as well as designing efficient, bright, and biocompatible XLCT imaging probes [15–18].

XLCT imaging can be performed using different x-ray beam geometries; each with their own advantages and disadvantages. Selective beam based XLCT is performed using a narrow x-ray beam that raster scans across the sample in a manner like the first-generation computed tomography (CT) scanners. This allows for very high-spatial resolution, since the beam size and location can be used as *a priori* information in the image reconstruction. The drawback of this method is the inherently long scan time due to the small excitation region and time needed to traverse the whole object. Another geometry is the fan or planar beam geometry, which can be used for imaging an entire cross-section at one time and allows for selective-planar imaging [11, 12]. This method eliminates the need for raster scanning which improves the imaging time, however, the lateral spatial resolution is degraded compared with the narrow beam selective excitation, since the excitation is no longer localized to a small region, but rather the entire cross section. The last x-ray beam geometry is the conical-beam geometry [13] which offers the fastest scanning time of the three geometries mentioned since the object is entirely excited by the beam at one time. However, this further compromises spatial resolution as a tradeoff. Due to advantages of improved spatial resolution, our efforts have been focused on the narrow x-ray beam based XLCT imaging. We originally explored narrow x-ray beam based XLCT imaging using collimators to generate a fine x-ray beam and used an EMCCD camera to detect the optical photons that reach the object surface [3–6, 19]. Using this method, we achieved promising results and demonstrated that we could separate targets with an edge-to-edge (EtE) distance of 0.4 mm [5] and could perform XLCT imaging at depths greater than 2 cm and at concentrations of 0.01 mg/mL (GOS:Eu^{3+} contrast agent) [19]. To improve on the imaging time, a challenge for the narrow-beam based XLCT, we have also proposed the idea of multiple beam

scanning using multiple-pinhole collimator [6] which reduced the imaging time by a factor equal to the number of x-ray beams. Another method we have explored, more recently, is using both a higher-flux x-ray beam as well as more sensitive optical detectors to perform XLCT imaging. Collimation, while easy to implement, is highly inefficient as only a small number of the generated x-ray photons can pass through the pinhole and the rest of the signal is absorbed by the collimator. We have recently demonstrated that by using x-ray optics (e.g. polycapillary lens), to generate a focused x-ray beam with a dual-cone geometry, we can perform much more sensitive XLCT imaging due to the increased x-ray photon flux. Also, instead of an EMCCD camera, using photo-multiplier tubes (PMTs), we can acquire our optical signal much more quickly and with a higher signal-to-background ratio (SBR) [7].

Rare earth elemental nanophosphors are promising XLT contrast agents for noninvasive bioimaging- such as to detect tumors *in vivo*. For such applications, the nanophosphors should ideally be small, colloidally stable, and chemically functionalizable for targeting, and generate bright radioluminescence signals with tissue penetrating red or near infrared light. Many microphosphors are commercially available, mostly developed for lighting, display, and x-ray imaging applications. Smaller stable nanophosphors have also been developed for biolabeling applications, especially fluorescence and upconversion, and some of these (e.g., $NaGdF_4$:Eu and Gd_2O_2S: Eu) are also good XLI contrast agents. Reducing the phosphor size usually decreases their luminescence yield due to quenching from surface defects and escape of x-ray generated photoelectrons, but annealing processes can help by reducing quenching from defects. Based on our previous work with XLCT imaging, along with the efforts of our collaborators, we have proposed and are currently building a small-animal dedicated focused x-ray luminescence tomography (FXLT) imaging system that also incorporates a microCT scanner. We will also synthesize nanophosphors with various emission wavelengths to be used as contrast agents for multiplexed XLCT imaging. Lastly, we also propose a deep-learning based XLCT reconstruction algorithm to improve upon our existing reconstruction methods. The remainder of the paper is arranged as follows. In Section 2, we discuss the design and build of our designed FXLT imaging system and the proposed scanning scheme. In Section 3, we discuss the proposed synthesized nanophosphors. In Section 4, we discuss the deep-learning based XLCT reconstruction algorithm and numerical simulations. Then in Section 5, we show the phantom experimental set-up for testing the proposed deep-learning based reconstruction algorithm. Lastly in Section 6, we discuss our results and conclude our paper.

2. FXLT Imaging System Design and Scanning Scheme

Figs. 1 and 2 below show computer-aided design (CAD) models of our FXLT scanner. The imaging system frame is built from extruded T-slotted aluminum bars (80/20 Inc.) and has approximate dimensions of 2.82" × 3.90" × 5.77" (width × length × height). Custom lead-lined stainless-steel panels and door (as seen in Fig. 1a) were designed and fabricated (BFK Innovation Inc.) and are mounted to the frame to protect from x-ray leakage as well as allowing for the system to be lighttight. The primary imaging system components are fixed onto a custom cut optics board that is mounted onto a heavy-duty ring track (HDRT) (Hepco Motion) mounted to the imaging system frame (Figs. 1b and 2). The HDRT has a central

bore diameter of 650 mm and contains an internal V-track that uses a pinion and shaft system to rotate for different angular projections. We will use a powerful servo-motor (Clearpath, Teknic) to drive the pinion. As seen in Figs. 1b and 2, a linear stage is used to position and bring our imaged object into the field-of-view (FOV) of the scanner components that are mounted to the HDRT. First, the object enters the FOV of the microCT scanner. For the microCT scanner, we have an x-ray tube (XTF5011, Oxford Instruments) fixed to an aluminum bracket. Opposite of the x-ray tube, we mount an x-ray detector (Shad-o-Box 1K HS, Teledyne DALSA) to collect our microCT projection images. We also fix the power supply (Shasta Power Supply) to the ring track as well. Following the microCT scan, the object is then positioned into the FOV of the FXLT scanner to perform x-ray optical imaging. Here, we use a powerful focused x-ray tube with polycapillary lens (fleX-Beam, XOS) that has an approximate focal spot size of 49.9 μm (FWHM, Mo-K_α[17.4 keV]) and a photon flux of 2.8×10^7 photons/sec (at 50 keV). The x-ray beam convergence angle is less than 2 degrees and the beam diameter changes to a maximum of 75 μm within a 10 mm range of the focal spot. The power supply (PCS-50) is fixed and mounted to the ring track. The x-ray tube is fixed onto a heavy-duty precision linear stage (NLS-8, Newmark Systems Inc.) that allows for translational scanning of the focused x-ray beam. Directly opposite of the polycapillary lens, we fix a small scintillator crystal (e.g. Ce: Lu_2SiO_5) that can constantly track the intensity of the focused beam by delivering the signal to a PMT through an optical fiber bundle. This can be used to determine when an object (i.e. Phantom) is in the path of the x-ray beam for boundary determination during image reconstruction. During the FXLT scans, any emitted optical photons that reach the object surface is delivered to an array of four PMTs (H7422-50, Hamamatsu Inc.) by use of two bifurcated liquid-light guides (Series 380, Lumatec) that are optimized for the NIR range (up to 800 nm) with high-efficiency. During the FXLT scans, the light guides are fixed and do not rotate. Before the optical signal is delivered to the PMTs, we can apply a bandpass filter in order to select two wavelengths (up to four) of interest as well which allows for us to perform multiplexed imaging. Then the PMT output signal is further amplified by use of a preamplifier (SR445A, Stanford Research Systems) and then a low-pass filter applied (BLP-10.7+, Cutoff Frequency: 11 MHz, Mini-Circuits) to reduce high-frequency noises before the signal is finally collected by a high-speed digitizer (DTS5730S, CAEN Technologies Inc.) connected to a lab computer. Fig. 3 summarizes the scanning scheme of the FXLT scanner schematically.

3.   X-ray Excitable Contrast Agents

Optically distinct rare earth elemental nanophosphors are proposed to be employed as contrast agents in this multiplexed bioimaging system. For example, $NaGdF_4$:Eu or Tb were synthesized using a citrate method, involving lanthanides-citrate complex formation followed by nucleation and growth upon the addition of NaF. Synthesized nanoparticles were washed and finally dispersed in aqueous pH 7 solution. Followed by synthesis, the nanoparticles are annealed at high temperature (above 850 °C) to increase the emission intensity by removing defects which can cause luminescence quenching. Also, to prevent particles sintering during annealing $NaGdF_4$ nanoparticles are enclosed with a silica shell using the method of Stöber process. The synthesized nanoparticles are characterized using

dynamic light scattering (DLS), transmission electron microscopy (TEM), and x-ray excited optical luminescence (XEOL) spectroscopy (Fig. 4).

Next, $NaGdF_4$ nanoparticles were encapsulated with silica layers, modified with (3-aminopropyl)triethoxysilane (APTES), and lastly functionalized with carboxylic acid—PEG—Biotin (1000 Da) using EDC coupling chemistry in aqueous MES buffer. The surface functionalization with biotin was initially verified by scanning electron microscopy (SEM) imaging which exhibits biotinylated nanophosphors have adhered to streptavidin-coated silica microspheres. Surface charge and size of the biotinylated nanophosphors were measured using DLS.

Synthesized nanoparticles emit visible light photons when irradiated with x-ray. The DLS measurement and TEM imaging indicate that the size of the nanophosphors without any modifications is around 100 nm. According to XEOL spectroscopy measurements, both Eu and Tb doped $NaGdF_4$ nanophosphors show low emission intensity, likely due to lack of luminescent centers or self-quenching, respectively. Later, hydrothermal treatment increased the emission intensity by a factor of 2 to 3 (annealing without a silica shell increased the emission intensity by another factor of 5 but resulted in sintered particles, negating their biological application). After annealing silica-coated $NaGdF_4$ particles, there is a minimal increase in intensity compared to pristine nanoparticles. Later, silica shelled nanophosophors were functionalized with biotin-labelled PEG molecules. Post functionalization steps, the nanophosphors bind well with a streptavidin-coated substrate (air-filled buoyant glass beads, Akadeum Life Sciences).

4. Machine Learning Based XLCT Reconstruction Algorithm

4.1 X-ray luminescence imaging model

X-ray luminescence imaging model incorporates x-ray attenuation, NIR light absorption and scattering. The image reconstruction is to localize and quantify a nanophosphors concentration distribution in a small animal. The propagation of light through the biological tissue is a complex process, which experiences both absorption and scattering simultaneously. A light propagation model describes the interaction of photons with scattering and absorbing media, and is essential for optical tomographic imaging. The radiative transfer equation (RTE) is an accurate model for photon propagation in biological tissues, and can be solved with a numerical solution or Monte Carlo simulation. From photon propagation model, we can express photon fluence rates on an object surface in terms of a Green function [22, 23]:

$$\phi(r) = \int \int \int G(r|r')S(r')dr' \quad r \in \partial \Omega, \tag{1}$$

where Ω is imaging region of interest, r is a positional vector, $\Phi(r)$ the photon fluence rate at a location r [Watts/mm^2], $S(r)$ the intensity of the NIR light source [Watts/mm^3] in the object. The intensity of NIR light emitted from nanophosphors is related to the nanophosphor concentration $\rho(r)$ to be reconstructed, the x-ray intensity distribution $X(r)$ in the imaging object which is determined by the Beer Lambert Law, and the NIR light yield η

of the nanophosphors which is defined as the quantum yield per unit nanophosphor concentration [2]: $S(r) = \eta X(r)\rho(r)$. Eq. (1) can be discretized into a matrix equation linking the nanophosphor distribution $\rho(r)$ and the NIR photon fluence rate $\Phi(r)$ at measurable position r [24, 25],

$$\phi = A \cdot \rho, \tag{2}$$

where A is the weight matrix of nanophosphor distribution. Eq. (2) describes a linear relationship between the nanophosphors concentration and measured NIR data. In the image reconstruction, we assume x-ray is a pencil beam, and NIR light source $S(r)$ only distributes on the pencil beam path. Nanophosphors concentration distribution can be reconstructed using an iterative image reconstruction algorithm with the minimization of the image total variation (TV).

4.2 Projection data synthesis

For enhancing scanning efficiency of the XLCT imaging, an important method is to reduce projection views and number of x-ray pencil beam translation. Here, we develop a data synthesis method of projection views from measured few-view data based on deep learning techniques to significantly enhance image quality of image reconstruction. Deep learning is an efficient method of functional approximation based on a training dataset to construct a nonlinear mapping from low quality images (reconstructed nanophosphors concentration images) to corresponding high quality images. We apply the residual neural network (ResNet) to modeling the non-linear mapping. ResNet is an advanced network architecture, which has the ability to obtain high-accuracy results for image processing. With use of identity shortcut, ResNet alleviates overfitting, reduces vanishing gradient problem, and allows the neural network converge faster and more efficiently. Our residual network consists of one convolution layer with 64 filters of 3×3 kernels, followed by four residual blocks, two convolution layers with 64 filters of 3×3 kernels, and one convolution layer with 32 filters of 3×3 kernels. Each layer is followed by a ReLU activation function. The last layer generates only one feature map with a single 3×3 filter as the output. Each residual block performs feed forward neural networks with shortcut connections that skip one or more layers. The network is trained using paired few-view projection data and full-view projection data. Through data training, ResNet generates a nonlinear mapping from measured projection data to a new projection data with minimization of the cost function. The network model under particular kernels and weights is calculated through forward propagation on a training dataset, and learnable parameters are updated according to the loss value through an optimization algorithm called backpropagation, which uses the chain rule to speed up the computation of the gradient for the gradient descent (GD) algorithm.

4.3 Training dataset

In the numerical simulation, the x-ray source voltage and current were set to 40 keV and 30 mA, respectively, and the x-ray beam was filtered with 0.5 mm A1 to filter out low energy photons. The optical properties of the cylindrical phantoms were set to the scattering coefficient of 15 cm^{-1} and the absorption coefficient of 0.5 cm^{-1}. An x-ray pencil beam was incident on the phantom to excite nanophosphors to emit NIR light, and three optical fiber

bundles equiangular distributed upper surface of the phantom to collect NIR. The x-ray pencil beam was translated with an increment of 0.5 mm in X-Y plane for 50 times to scan the phantom for a projection view. We establish 400 phantoms with random positions and size target regions to generate training dataset based on x-ray luminescence imaging model described by Eqs. (1–2). The projection data was formed from the NIR measurements at an angular view. The few-view projection data are generated with an angular step size of 12 degree for 15 angular projections over 180°. The full-view projection data are generated with an angular step size of 6 degree for 30 angular projections over 180°.

4.4 Testing of the proposed algorithms with numerical data

We performed testing to demonstrate the proposed deep learning-based image reconstruction method based on an optically 3D digital cylindrical phantom. Four target regions were implanted in the phantom. An x-ray pencil beam was incident on phantom at an X-Y plane to excite nanophosphors to emit NIR light, and three optical fiber bundles equiangular distributed upper surface of the phantom to collect NIR. The x-ray pencil beam was translated with an increment of 0.5 mm in X-Y plane for 50 times to obtain NIR light intensity at each projection view. Then the iterative image reconstruction algorithm with the minimization of the image total variation (TV) was applied to reconstruct nanophosphors concentration distribution. Our results have shown that the proposed ResNet can effectively reduce noise and artifacts, and improve spatial resolution images, as shown in Fig. 5. The peak signal-to-noise ratio (PSNR) and structural similarity (SSIM) are utilized to quantitatively evaluate the performance of the deep learning image processing methods, achieving PSNR of 24.09 and SSIM of 0.7993 for representative slices, while the image reconstructed with few view projection data have PSNR of 19.48 SSIM of 0.6968.

5. Phantom Experiments for Machine Learning Based XLCT Reconstruction Algorithms

In order to test and verify the performance of our proposed machine-learning based XLCT reconstruction algorithm, we have performed a set of twenty XLCT scans (also microCT scans (Fig. 6)) with various target set-ups using our prototype focused x-ray beam based XLCT imaging system in [7]. Twenty cylindrical phantoms were created with the same geometry (12 mm diameter and 20 mm height) and composition (2% agar, 1% intralipid, and water) and were embedded with various targets in different arrangements as seen in Fig. 6 from the microCT reconstructed images, including a single phantom with no target (background phantom, Fig. 6(e,4)). Targets were composed of GOS:Eu^{3+} particles (UKL63/UF-R1, Phosphor Tech. Ltd.) at a concentration of 10 mg/mL in a similar background solution. Fig. 6 row (a) show the single target cases with each of the various target sizes used. A single case using a large target (4.60 mm) was created using a target mold and was embedded as shown in Fig. 6(a, 1). The other targets were created by injecting the target solution into capillary tubes which were then embedded into the phantom. Capillary tubes with outer diameters (O.D.)/inner diameters (I.D.) of 2.0/1.0 mm (Thomas Scientific), 0.8/0.4 mm (Drummond Scientific), and 0.4/0.2 mm (Drummond Scientific) were used as can be seen in Fig. 6 (a, 2), (a, 3), and (a, 4) respectively (the I.D. is considered

to be the target size). After the single target cases, more multiple target cases were created as seen in Fig. 6 (rows (b)-(e)).

Each of the phantoms were scanned inside of our XLCT imaging system as described in [7]. In short, high-energy x-ray photons are generated by an x-ray tube (X-Beam, XOS) and focused with a polycapillary lens to a focal spot size of approximately 101.5 μm which is where the phantom stage was placed. The x-ray beam size changes to a maximum of 150 μm within the phantom scanning region. Opposite of the x-ray beam, an x-ray detector (Shad-o-Box 1024, Teledyne DALSA) tracks the x-ray beam intensity for boundary purposes. The phantom stage sits on top of a manual lab jack (LJ750/M, Thorlabs) which allows us to manually adjust the x-ray beam scanning depth. In this case, we used an x-ray beam scanning depth of 5 mm (distance from the top surface of the phantom). The jack is on top of both a rotary stage (B4872TS-ZR, Velmex Inc.) and linear stage (Unislide MA40, Velmex Inc) which allows us to acquire measurements from different linear positions and at different angles. A single optical fiber bundle was positioned 90 degrees from the x-ray beam and rotated with the phantom during measurements. During the XLCT scans, any emitted optical photons that reach the side surface was collected by the fiber bundle and then delivered to a sensitive fan-cooled PMT (H7422-50) from which the signal is then sent to a preamplifier (SR445A) for signal amplification, then a low-pass filter (BLP-10.7+), before being collected by a high-speed oscilloscope (MDO3104, Tektronix) and saved to a lab computer. For all XLCT scans, we acquired XLCT measurements using an x-ray beam step size of 0.150 mm with a total of 80 steps to traverse the entire phantom and took measurements at 12 angular projections (15°/projection) using an acquisition time of 100 ms total for each step. For all measurements, the x-ray tube was operated at 30 kV and 0.5 mA (15 W). Immediately following the XLCT scans, the microCT scans (shown in Fig. 6) were performed in a separate microCT scanner as described in [19].

Fig. 7 below shows a typical XLCT reconstruction using our previous algorithm as detailed in [4, 26–29] without the use of machine-learning algorithm for the phantom shown in Fig. 6(a, 2) embedded with a 1.0 mm diameter target. Using the microCT reconstructed image (Fig. 7a), both the phantom and target center positions were determined, and then the distance from the center is used as the ground truth location in the XLCT reconstruction. For our XLCT reconstruction using our usual method [27–29], we obtained a DICE similarity coefficient of 90.9% (closer to 100% is ideal). Due to time constraints, we will show the results of the machine-learning based XLCT reconstructions in the oral presentation.

6. Discussion and Conclusions

XLCT has become an attractive imaging modality for the 3D high-spatial resolution imaging of deeply embedded x-ray excitable contrast agents with good measurement sensitivity. Overall in this work, we have proposed and designed a small-animal dedicated FXLT scanner, synthesized NaGdF$_4$ nanophosphors with unique emission spectra, proposed a deep-learning based XLCT reconstruction algorithm and have shown our preliminary results from these three aspects in this study. Here, we have shown the design of our small-animal dedicated FXLT scanner that can perform both microCT imaging and 3D high-resolution XLCT imaging in one system. Having both the ability to perform the microCT imaging

immediately before the XLCT imaging inside a single scanner is highly beneficial and allows for easier registration of the anatomical and optical imaging since the orientation of the object is guaranteed to be the same. With our previous setup, having to move the object to two different scanners for the imaging made it harder to ensure both CT and XLCT are scanned in the same orientations. A few other additions to the FXLT scanner will also allow for improved imaging performance compared with our prototype system [7]. First, the x-ray beam size of the new scanner is much smaller than the previous (49.9 μm vs 101.5 μm) which will allow for higher spatial resolution capabilities. From our previous reports [5, 20–21], we can estimate the spatial resolution of the designed FXLT scanner to be about 94 μm. Next, the use of four highly sensitive PMTs (H7422-50) to detect the emitted optical signals will allow for much more sensitive set-up than previously where only one PMT was used. In addition, we have recently switched from silica core optical fiber bundles to liquid-light guides which allow for much higher optical transmission efficiency, especially in the NIR range which means we expect much more signal to be delivered to each PMT than previously. From our previous study regarding the sensitivity of XLCT for GOS:Eu^{3+}, we estimated that the limits of detection (LOD) was approximately 2 μg/mL. With this new setup, we expect to achieve an even lower LOD which will be verified in future studies. With additional PMTs, we are also capable of performing imaging of different nanoparticles with different emission wavelengths as well which can be useful for multiplexed imaging of different targets.

We have also synthesized 100 nm NaGdF$_4$ (both Eu and Tb doped) nanophosphors with a silica coating and functionalized with biotin. These particles have distinct luminescence spectra compared to previous Gd$_2$O$_2$S particles, which will allow multi-color XLCT imaging. Future work involves optimizing synthesis, annealing, and surface modification protocols to obtain brighter nanophosphors and mixing with Gd$_2$O$_2$S:Eu nanophosphors for multicolor imaging. After having nanospheres with brighter luminescence and longer stability their application will be tested as *in situ* light sources for detecting target receptor molecules *in vivo*.

Lastly, we have also proposed and developed a deep-learning based XLCT reconstruction algorithm, based on the residual neural network (ResNet). In our preliminary work shown here, we can see a clear enhancement in the XLCT reconstruction image quality (Fig. 5). Further testing (such as reconstruction of the phantom experiments detailed in Section 5) will be performed in order to further verify our proposed reconstruction method.

Acknowledgments

References

[1]. Pratx G, Carpenter CM, Sun C, Rao R, and Xing L, "Tomographic molecular imaging of x-ray excitable nanoparticles," Opt. Lett 35, 3345–3347 (2010). [PubMed: 20967061]

[2]. Pratx G, Carpenter CM, Sun C, and Xing L, "X-ray Luminescence Computed Tomography via Selective Excitation: A Feasibility Study," IEEE Trans. Med. Imag 29 (12), 1992–1999 (2010).

[3]. Li C, Di K, Bec J, and Cherry SR, "X-ray luminescence computed tomography imaging: experimental studies," Opt. Lett 38, 2339–41 (2013). [PubMed: 23811921]

[4]. Li C, Martinez-Davalos A, and Cherry SR, "Numerical simulation of x-ray luminescence computed tomography for small-animal imaging," J. Biomed. Opt 19, 046002 (2014). [PubMed: 24695846]

[5]. Zhang W, Zhu D, Lun M, and Li C, "Collimated superfine x-ray beam based x-ray luminescence computed tomography," J. X-ray Sci. Technol 25 (6), pp 945–957, (2017).

[6]. Zhang W, Zhu D, Lun M, and Li C, "Multiple pinhole collimator based x-ray luminescence computed tomography," Biomed. Opt. Expr 7 (7), 2506–23 (2016).

[7]. Zhang W, Lun MC, Nguyen A, and Li C, "A focused x-ray beam based x-ray luminescence computed tomography," J Biomed. Opt 22 (11), 116004 (2017).

[8]. Lun MC, Zhang W, Zhao Y, Anker JN, Cong W, Wang G, and Li C, "Development of a focused-X-ray luminescence tomography (FXLT) system," arXiv:1709.10186 [physics.med-ph] (Sept. 2017).

[9]. Cong W, Wang C, and Wang G, "Stored Luminescence Computed Tomography," Appl. Opt 53, 5672–5676 (2014). [PubMed: 25321362]

[10]. Cong W, Pan Z, Filkins RJ, Srivastava AM, Ishaque AN, Stefanov P, and Wang G, "X-ray micromodulated luminescence tomography in dual-cone geometry," J. of Biomed. Opt 19(7), 076002 (2014).

[11]. Cong W and Wang G, "X-ray fan-beam luminescence tomography" IEEE 11th International Symposium on Biomedical Imaging (ISBI), 1164–1167 (2014).

[12]. Quigley B, Smith CD, Cheng SH, Souris JS, Pelizzari CA, Chen CT, Lo LW, Reft CS, Wiersma RD, La Riviere PJ, "Sensitivity Evaluation and Selective Plane Imaging Geometry for X-ray Induced Luminescence Imaging," Med. Phys 44 (10), 5367–5377 (2017). [PubMed: 28703922]

[13]. Chen D, Zhu S, Yi H, Zhang X, Chen D, and Liang J, "Cone beam x-ray luminescence computed tomography: a feasibility study," Med. Phys 40 (3), 031111 (2013). [PubMed: 23464291]

[14]. Cong W, Shen H, and Wang G, "Spectrally resolving and scattering compensated x-ray luminescence/fluorescence computed tomography," J. Biomed. Opt 16, 066014 (2011). [PubMed: 21721815]

[15]. Sudheendra L, Das GK, Li C, Stark D, Cena J, Cherry SR, and Kennedy IM, "NaGdF$_4$:Eu^{3+} Nanoparticles for enhanced x-ray excited optical imaging," Chem. Mater 26, 1881–1888, (2014). [PubMed: 24803724]

[16]. Chen H, Wang F, Moore TL, Qi B, Sulejmanovic D, Hwu SJ, Mefford OT, Alexis F, Anker JN, "Bright X-ray and up-conversion nanophosphors annealed using encapsulated sintering agents for bioimaging application," J. Mater. Chem. B, 5, 5412 (2017) [PubMed: 29497532]

[17]. Gao T, Lin Y, Zhang WJ, Hong JS, Lin RH, Wu XP, Li J, Lu CH, and Yang HY, "High-efficiency X-ray luminescence in Eu^{3+}-activated tungstate nanoprobes for optical imaging through energy transfer sensitization", Nanoscale 10, 1607 (2018). [PubMed: 29323363]

[18]. Zhang W, Shen Y, Liu M, Gao P, Pu H, Fan L, Jiang R, Liu Z, Shi F, and Lu H, "Sub-10 nm water-dispersible β-NaGdF$_4$:X% Eu^{3+} nanoparticles with enhanced biocompatibility for in vivo x-ray luminescence computed tomography," Appl. Mater. Interfaces 9, 29985–399993 (2017).

[19]. Lun MC, Zhang W, and Li C, "Sensitivity study of x-ray luminescence computed tomography," Appl. Opt 56 (11), 3010–3019 (2017). [PubMed: 28414356]

[20]. Zhang Y, Lun MC, Li C, and Zhou Z, "Method for improving the spatial resolution in narrow x-ray beam based x-ray luminescence computed tomography," J. Biomed. Opt 24 (8), 086002 (2019).

[21]. Lun MC and Li C, "Focused X-ray Luminescence Computed Tomography," Proc. SPIE 11113, Developments in X-Ray Tomography XII, 111131B (2019).

[22]. Chen J, Fang Q, Intes X. Mesh-based Monte Carlo method in time-domain widefield fluorescence molecular tomography. J. Biomed. Opt 17(10):106009 (2012). [PubMed: 23224008]

[23]. Wang G, Cong W, Durairaj K, Qian X, Shen H, Sinn P, et al. In vivo mouse studies with bioluminescence tomography. Opt. Express. 14(17):7801–9 (2006) [PubMed: 19529149]

[24]. Cong W, Wang G, Kumar D, Liu Y, Jiang M, Wang LV, et al. Practical reconstruction method for bioluminescence tomography. Opt. Express. 13(18):6756–71 (2005). [PubMed: 19498692]

[25]. Cong W, Shen H, Wang G. Spectrally resolving and scattering-compensated x-ray luminescence/ fluorescence computed tomography. J. Biomed. Opt 16(6):066014 (2011) [PubMed: 21721815]

[26]. Zhu D, Zhao Y, Baikejiang R, Yuan Z, and Li C, "Comparison of regularization methods in fluorescence molecular tomography", Photonics, 1, 95–109 (2014).

[27]. Zhu D and Li C, "Nonconvex regularizations in fluorescence molecular tomography for sparsity enhancement," Phys. Med. Biol 59, 2901–2912 (2014). [PubMed: 24828748]

[28]. Zhu D and Li C, "Nonuniform update for sparse target recovery in fluorescence molecular tomography accelerated by ordered subsets," Biomed. Opt. Express 5, 4249–4259 (2014). [PubMed: 26623173]

[29]. Zhu D and Li C, "Accelerated image reconstruction in fluorescence molecular tomography using a non-uniform updating scheme with momentum and ordered subsets methods," J. Biomed. Opt 21, 016004 (2016).
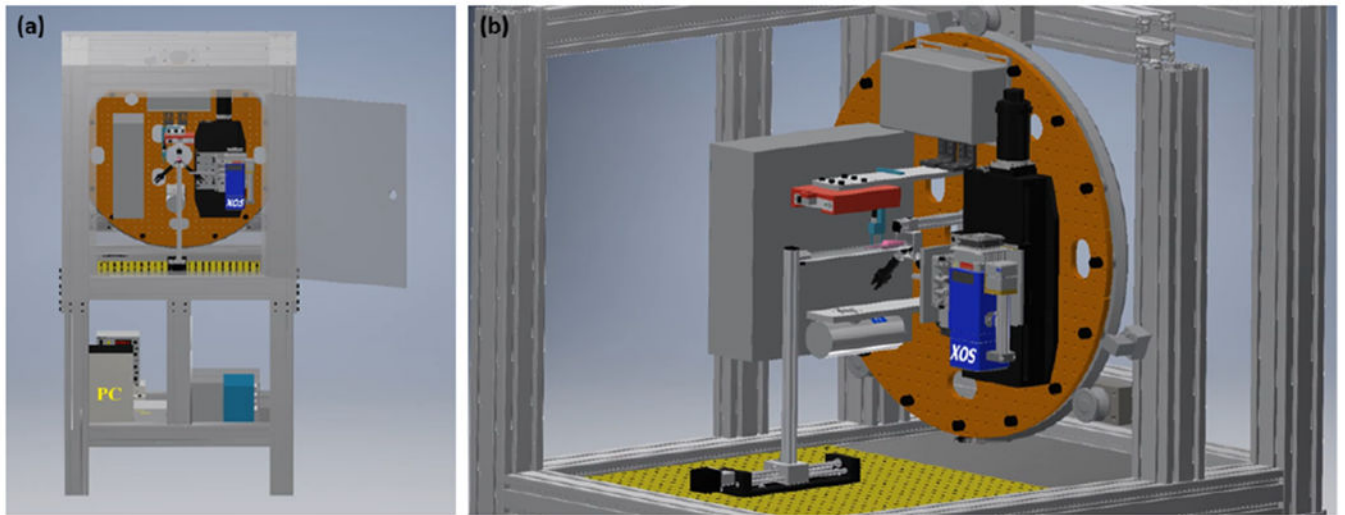
Fig. 1.
CAD model of FXLT Imaging System. (a) Full frontal view with radiation shielding panels and door made transparent; (b) Zoomed-in corner view with radiation panels removed.
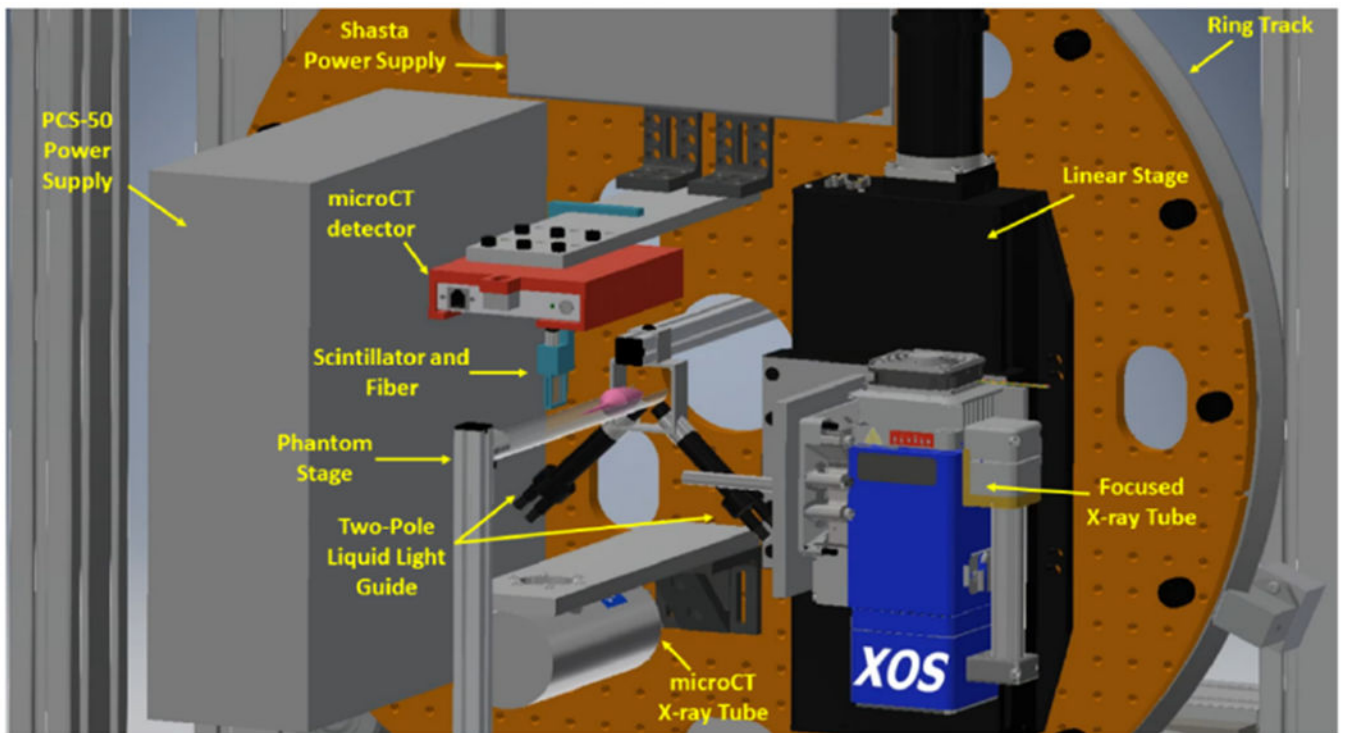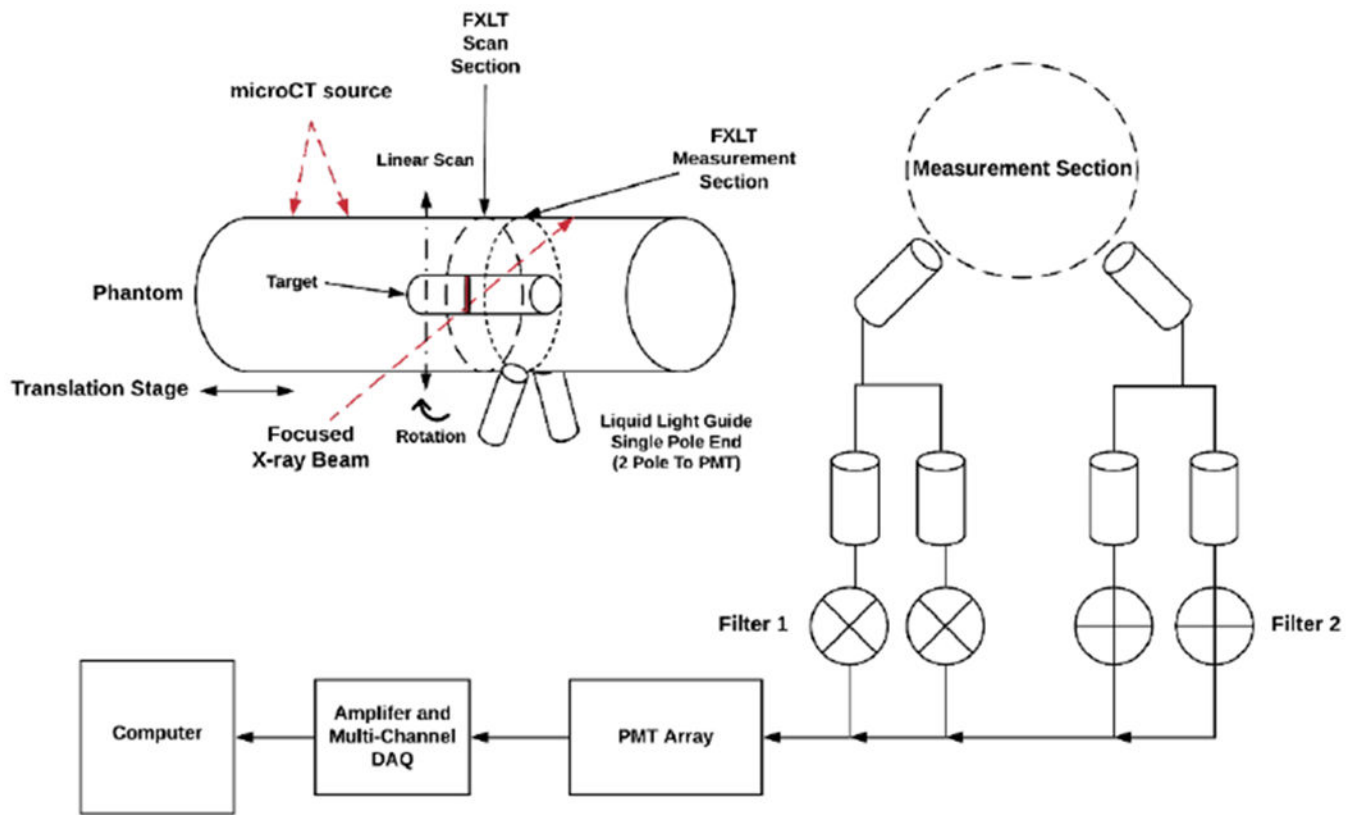
Fig. 2.
Main FXLT imaging components with labels.

Fig. 3.
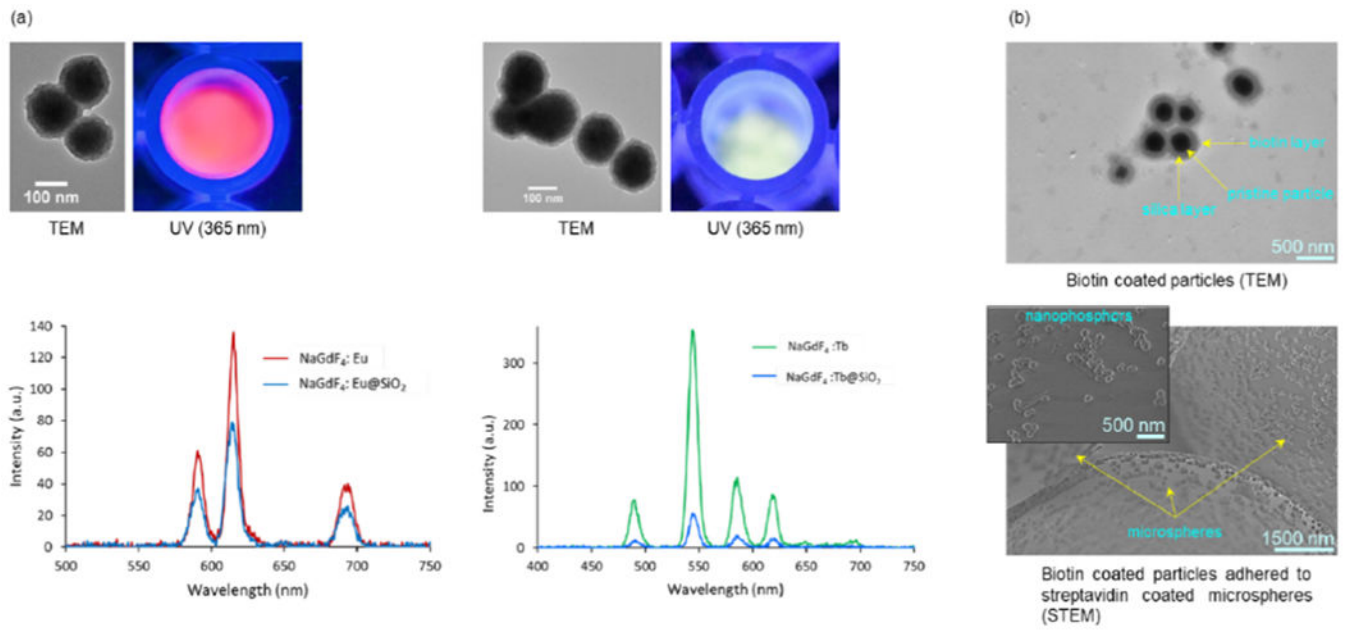Proposed scanning scheme and acquisition for FXLT imaging system.

Fig. 4.
(a) Luminescence spectra of NaGdF$_4$:Eu (red) and NaGdF$_4$:Tb (green) nanophosphors, TEM images above the spectra show silica coated particles. (b) TEM image of biotin coated nanophosphors (top), and STEM image of biotin coated nanophosphors adhered to streptavidin coated microspheres (bottom), inset image is a closer view.
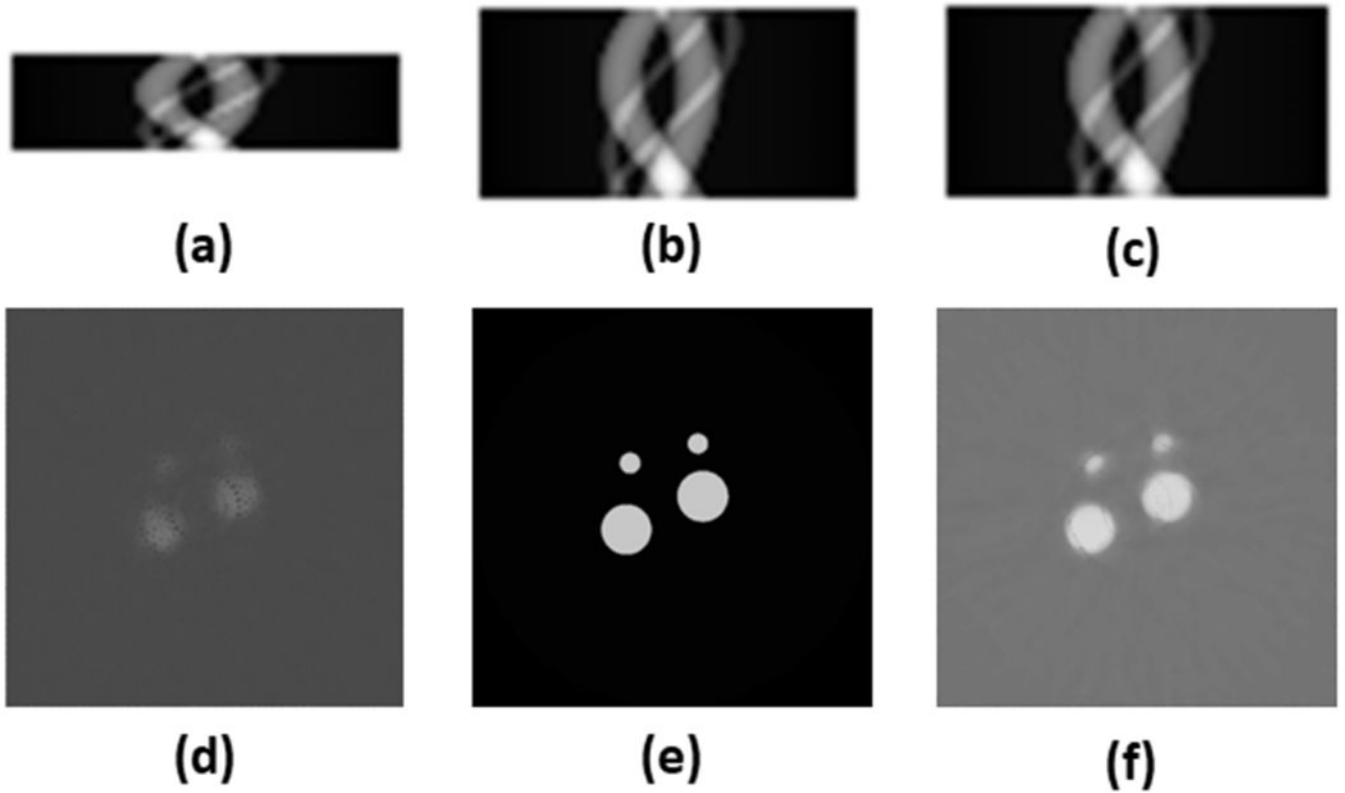
Fig. 5.
Projection data synthesis and image reconstruction. (a) Sinogram of 15 projection views; (b) Sinogram of 30 projection views; (c) Reconstructed sinogram from 15 projection views; (d) Image reconstructed from 15 projection views; (e) Ground truth image of phantom at a plane; (f) Image reconstructed from reconstructed 30 projection views.
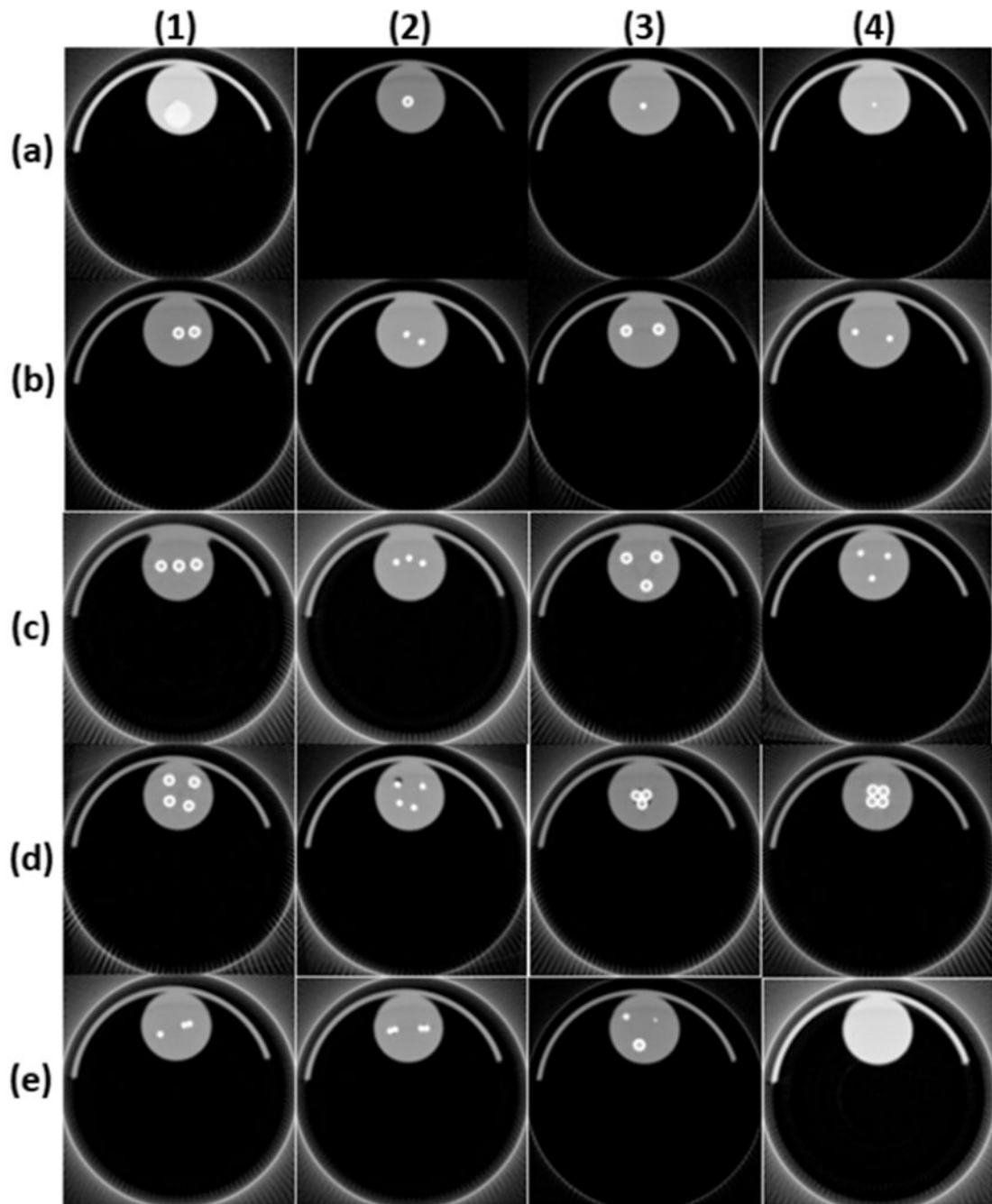
Fig. 6.
microCT scans of the phantoms used to test the proposed machine-learning based XLCT reconstruction algorithm. Slices are taken 5 mm from the top surface of the phantom which is the same as the x-ray beam scanning section.
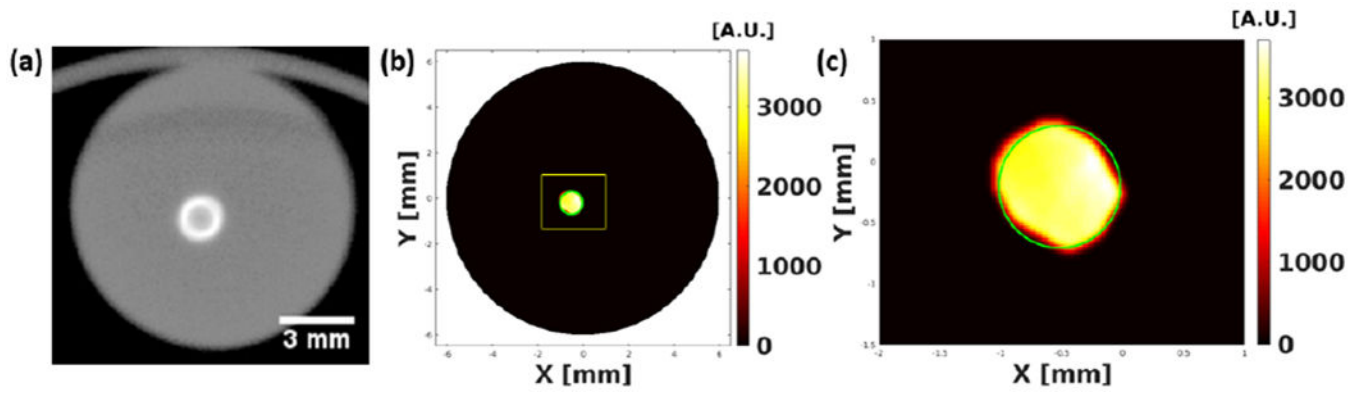
Fig. 7.
Typical XLCT reconstruction case without Machine Learning Algorithm using Phantom corresponding to Fig. 6 (a, 2). (a) Cropped microCT reconstructed image of scanned section; (b) XLCT reconstructed image; (c) Zoomed-in XLCT reconstruction of target area (Yellow Box in (b)).